Received: 1 January 2025 | Revised: 14 April 2025 | Accepted: 15 April 2025

DOI: 10.1002/pro.70142

RESEARCH ARTICLE

THE PROTEIN SOCIETY WILEY

Hierarchy in regulator interactions with distant transcriptional activation domains empowers rheostatic regulation

Amanda D. Due[1,2,3] | Norman E. Davey[4] | F. Emil Thomasen[2,3] | Nicholas Morffy[5] | Andreas Prestel[1,2,3] | Inna Brakti[1,2,3] | Charlotte O'Shea[1,2] | Lucia C. Strader[5] | Kresten Lindorff-Larsen[2,3] | Karen Skriver[1,2] | Birthe B. Kragelund[1,2,3]

[1]REPIN, University of Copenhagen, Copenhagen, Denmark

[2]Linderstrøm-Lang Centre for Protein Science, University of Copenhagen, Copenhagen, Denmark

[3]Structural Biology and NMR Laboratory, Department of Biology, University of Copenhagen, Copenhagen, Denmark

[4]Division of Cancer Biology, The Institute of Cancer Research, London, UK

[5]Department of Biology, Duke University, Durham, North Carolina, USA

Correspondence
Karen Skriver, REPIN, University of Copenhagen, DK-2200 Copenhagen, Denmark; Linderstrøm-Lang Centre for Protein Science, University of Copenhagen, DK-2200 Copenhagen, Denmark.
Email: kskriver@bio.ku.dk

Birthe B. Kragelund, REPIN, University of Copenhagen, DK-2200 Copenhagen, Denmark; Linderstrøm-Lang Centre for Protein Science, University of Copenhagen, DK-2200 Copenhagen, Denmark; Structural Biology and NMR, Laboratory, Department of Biology, University of Copenhagen, DK-2200 Copenhagen, Denmark.
Email: bbk@bio.ku.dk

Funding information
Lundbeck Foundation, Grant/Award Number: R155-2015-2666; Natur og Univers, Det Frie Forskningsråd, Grant/Award Number: 9040-00164B; Cancer Research UK Senior Cancer Research Fellowship, Grant/Award Number: C68484/A28159; Novo Nordisk Fonden, Grant/Award Numbers: NNF18OC0032996, NNF18OC0033926, NNF22OC0079339

Review Editor: Aitziber L. Cortajarena

Abstract

Transcription factors carry long intrinsically disordered regions often containing multiple activation domains. Despite numerous recent high-throughput identifications and characterizations of activation domains, the interplay between sequence motifs, activation domains, and regulator binding in intrinsically disordered transcription factor regions remains unresolved. Here, we map sequence motifs and activation domains in an *Arabidopsis thaliana* NAC transcription factor clade, revealing that although sequence motifs and activation domains often coincide, no systematic overlap exists. Biophysical analyses using NMR spectroscopy show that the long intrinsically disordered region of senescence-associated transcription factor ANAC046 is devoid of residual structure. We identify two activation domain/sequence motif regions, one at each end that both bind a panel of six positive and negative regulator domains from biologically relevant regulators promiscuously. Binding affinities measured using isothermal titration calorimetry reveal a hierarchy for regulator binding of the two ANAC046 activation domain/sequence motif regions defining these as regulatory hotspots. Despite extensive dynamic intramolecular contacts along the disordered chain revealed using paramagnetic relaxation enhancement experiments and simulations, the regions remain uncoupled in binding. Together, the results imply rheostatic regulation by ANAC046 through concentration-dependent regulator competition, a mechanism likely mirrored in other transcription factors with distantly located activation domains.

KEYWORDS
activation domains, intrinsically disordered region, isothermal titration calorimetry, nuclear magnetic resonance, protein–protein interactions, short linear motif, transcription factor

1 | INTRODUCTION

Intrinsically disordered regions (IDRs) are conformationally malleable, empowering them with an enormous interaction potential in protein networks (Holehouse & Kragelund, 2023) and responsiveness to cellular cues through post-translational modifications (Newcombe et al., 2022) and interactions (Bjarnason et al., 2023). Short linear motifs (SLiMs) are short conserved sequence stretches (typically less than 10 residues) within an otherwise non-conserved context (Berlow et al., 2017; Davey et al., 2012; O'Shea et al., 2017). They are prevalent in IDRs, where they are responsible for interactions. Often, SLiMs fold upon binding to form short *α*-helices (Davey et al., 2012; Gianni et al., 2016; Rogers et al., 2014; Wright & Dyson, 2015) with large context effects on affinity, mostly arising from the flanking regions (Karlsson et al., 2022; O'Shea et al., 2017; Palopoli et al., 2018; Prestel et al., 2019). However, SLiMs that remain disordered in the complex also exist (Dreier et al., 2022).

Intrinsic disorder is pronounced in transcriptional processes (Christensen et al., 2019; Liu et al., 2006; Staby et al., 2017) and transcription factors are key players. They activate or repress target gene transcription by the recruitment of additional components of the transcriptional machinery including coregulators to the target gene (Kornberg, 2005). Transcription factors generally consist of at least a folded DNA binding domain, enabling binding to their *cis*-elements, and a transcriptional regulatory domain, which is often intrinsically disordered. Within these IDRs, activation domains (ADs) drive coactivator binding, thereby activating transcription (Udupa et al., 2024).

The identification of ADs and the decomposition of their sequence properties have been facilitated by numerous recent high-throughput screens conducted in multiple organisms (Broyles et al., 2021; Erijman et al., 2020; Hummel et al., 2023; Morffy et al., 2024; Staller et al., 2022). These show that transcription factors can carry more than one AD, and that neighboring ADs may retard regulator dissociation by allovalency involving recapturing of regulators from one AD through binding to another AD (Delaforge et al., 2025; Sanborn et al., 2021). The studies also showed that the AD strength, that is, the ability to activate transcription, depends on the density and patterning of different types of amino acid residues, for example, acidic and aromatic/leucine residues (Broyles et al., 2021; Erijman et al., 2020; Hummel et al., 2023; Staller et al., 2022). The acidic-aromatic patterning was suggested to be important for facilitating binding site accessibility in the transcription factors for coregulators (Kotha & Staller, 2023; Staller et al., 2022). The patterning often leads to structure formation of the AD upon complex formation (Lochhead et al., 2020). However, some studies also propose the formation of more dynamic complexes between ADs and coregulators (Tuttle et al., 2021). High-throughput affinity measurements of regulator:AD interactions revealed affinities in the nM–μM range with coregulator domains binding ADs either specifically or promiscuously (DelRosso et al., 2024). Furthermore, SLiMs were suggested to play a functional role in ADs primarily when the ADs fold upon binding (Sanborn et al., 2021). Although these recent studies have contributed to the understanding of aspects of AD:coactivator interactions such as specificity/promiscuity, multivalency, and the role of SLiMs, several of the studies have focused on AD interactions with the MEDIATOR subunit MED15 or with cAMP-response element binding (CREB)-binding protein (CBP)/p300 (DelRosso et al., 2024; Mindel et al., 2024; Sanborn et al., 2021). Therefore, more case studies with both different transcription factors and different regulators are needed to improve our understanding of transcription.

To decompose the molecular details of regulator:AD interactions, we linked data from a high-throughput AD screen (Morffy et al., 2024) with clade bioinformatics and experimental biophysical analyses of the *Arabidopsis thaliana* NAM, ATAF1/2, CUC (ANAC) transcription factor family, a plant-specific family with more than 100 members. Due to similar biological functions of the members in senescence and development (Gonçalves et al., 2015; Oda-Yamamizo et al., 2016) and to the intriguing patterns in their disorder profile (Stender et al., 2015) we focused on clade II-3 containing ANAC transcription factors. We identified the SLiMs of the clade and compared these with AD locations, revealing nonsystematic overlaps between SLiMs and ADs. Using ANAC046 as a representative, we thermodynamically and structurally characterized its interactions with a pool of biologically relevant regulators. The affinities and order of binding uncovered a promiscuous binding strategy with independence and hierarchy of the two distant ADs in the long IDR of ANAC046. These results suggest rheostatic regulation with little chemical specificity relying on concentration-dependent competition. We suggest that similar regulation mechanisms are mirrored in other transcription factors with distant ADs in long IDRs.

2 | RESULTS

2.1 | SLiM identification in the long IDRs of ANAC clade II-3 transcription factors

As a first step, we identified conserved sequence motifs in the ANAC clade II-3 transcription factors, members of which share regulatory functions (Stender et al., 2015). In the model plant *Arabidopsis*, this subgroup consists of 13 transcription factors, which all contain a folded NAC DNA binding domain (Figure 1a).

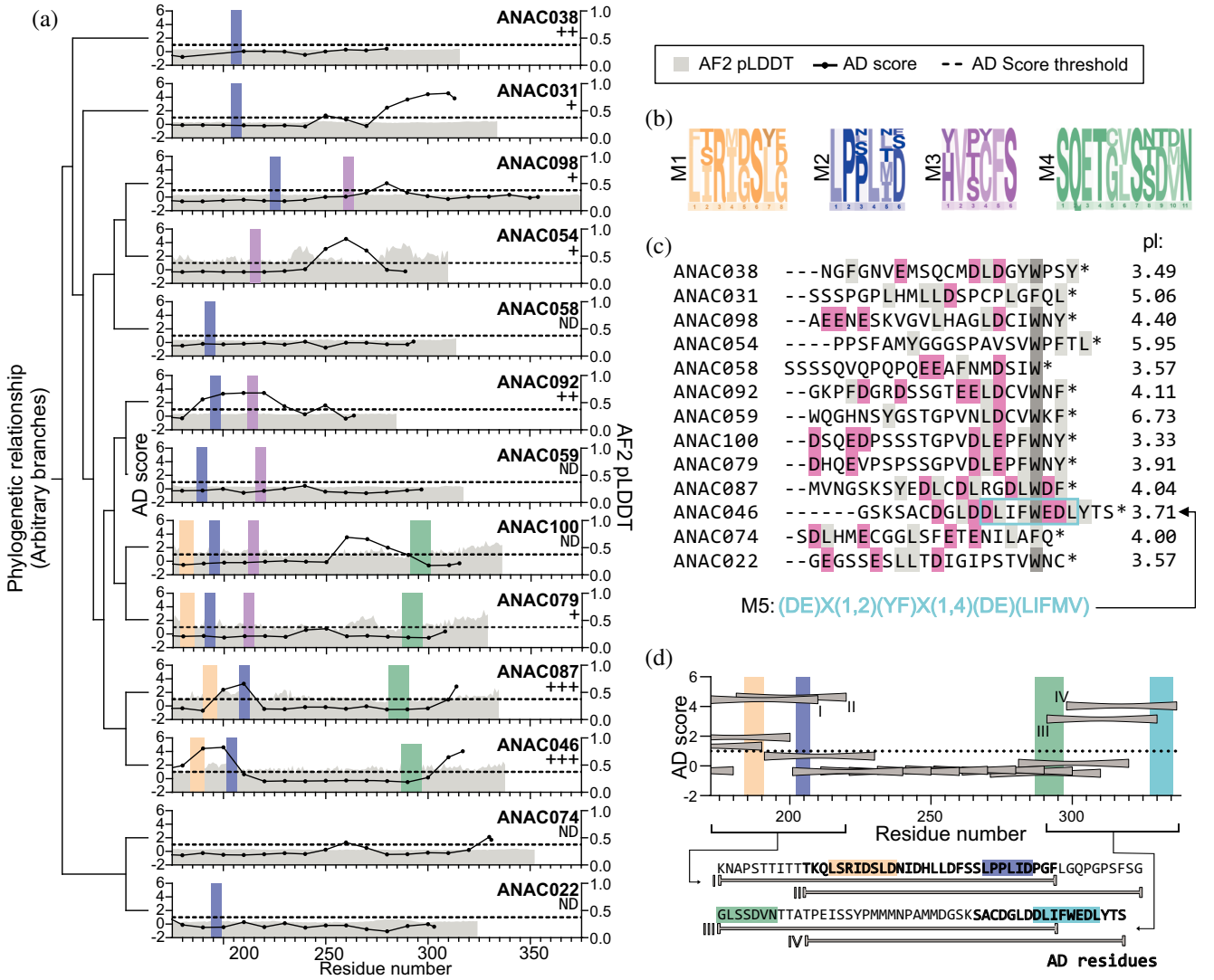

FIGURE 1 Identification of SLiMs and ADs in the ANAC II-3 subgroup. (a) Thirteen NAC transcription factors from *Arabidopsis* ordered by the phylogenetic relationship reported in Jensen et al. (2010). For each, the IDR is shown with SLiM mapping; M1 (yellow), M2 (purple), M3 (pink), and M4 (green). Scores from AD screens are shown as a line with dots at the tile center (40 residue length) (Morffy et al., 2024). AD threshold (dashed line) was defined as one standard deviation from the mean AD score of the full library in Morffy et al. (2024). Disorder is represented by normalized pLDDT scores in gray (<0.5 regarded as disordered). Below the names of each transcription factor, the transcriptional activity is indicated as minimally active (+), activator (++), and strong activator (+++) according to Hummel et al. (2023). (b) Logo plots of the four identified SLiMs generated based on the SLiM instances in (a) and colored as in (a). (c) Alignment of the last 21 residues from the transcription factors in (a) based on a single tryptophan (or phenylalanine) in the sequences. Aromatic or leucine residues are gray and acidic residues pink. The isoelectric points of the sequences are shown to the right. The sequence boxed in blue is the known SLiM for RCD1-RST (RIM, M5) binding shown below in light blue. (d) Tiles used in AD scoring of the ANAC046 IDR (Morffy et al., 2024). AD score threshold shown as dotted line and defined as one standard deviation from the mean AD score of the full library. Tiles I–IV are shown below for identification of the ADs (gray lettering), with the positions of M1–M4 highlighted.

The DNA binding domain is followed by a C-terminal region, differing in length, and with low AlphaFold (Jumper et al., 2021) confidence (pLDDT) scores suggestive of intrinsic disorder (Figure 1a) (Akdel et al., 2022). To identify SLiMs, we aligned the IDRs of each clade member individually with orthologous *viridiplantae* sequences and generated logo plots (Figure S1a). In this way, we identified four SLiMs (M1–M4) spanning 6–11 residues (Figure 1a, b). M2 and M3 were previously identified in some of the NAC transcription factors (Jensen et al., 2010; Taoka et al., 2004), but their functions remain elusive, while M1 and M4 were identified here (Figure 1b). M2 is the most frequently occurring SLiM present in 11 of the 13 transcription factors of clade II-3, while M3 is present in six members. M1 and especially M4, present in the same four members, are long and each may contain more than one SLiM.

To examine if the four SLiMs are present in additional *Arabidopsis* transcription factors, each SLiM was

screened against the *Arabidopsis* transcription factor proteome using PSSMSearch (Krystkowiak et al., 2018). The analyses (Tables S1–S4) revealed no additional instances of M3. For M1, M2, and M4, additional instances remained after filtering. For M1, instances were found in ANAC017 and ANAC016. M2 occurs in nine additional transcription factors. For M4, two separate analyses were performed using different filtering strategies. These revealed that M4 has four and 31 instances from different transcription factors depending on the SLiM consensus used in the filtering strategy (Table S4). Summing up, the IDRs of the ANAC clade II-3 transcription factors are rich in SLiMs (Figure 1a), but the expansion of their SLiMs outside this subgroup is limited except for M4.

2.2 | SLiMs are not directly linked to AD activity

To investigate whether the SLIMs overlap with ADs, we used data from a high-throughput yeast-based assay (Morffy et al., 2024), with the AD threshold μd as one standard deviation from the mean AD score of the full library (Figure 1a). Five clade members lack functional ADs, while ANAC087 and ANAC046 contain two ADs, and the rest of the transcription factors one identified AD. We found a link between transcription factors being strong activators (Hummel et al., 2023) and containing two experimentally identified ADs (Figure 1a) (Morffy et al., 2024). M1, M2, and M3 locate within ADs for some transcription factors, but not at the AD center, and there is no systematic overlap. Noticeably, an N-terminal AD detected for ANAC046 and ANAC087 was not identified for ANAC100 and ANAC079 even though all four contain both M1 and M2 in this region (Figure S1b). Combined, these analyses suggest either no direct involvement of SLiMs in AD activity or indirect involvement through regulatory modulation, for example, phosphorylation or binding of negative regulators.

The AD scores in the C-terminal region of some of the transcription factors exceeded the threshold value; hence, we examined the C-terminal sequences (Figure 1c). The 21 C-terminal residues of all transcription factors contain hydrophobic or aromatic residues (Figure 1c), and most are rich in acidic residues as reflected in low isoelectric points (Figures 1c and S3). ANAC046 contains a SLiM (here named M5) (Figure 1c) in its C-terminus, known as the Radical-Induced Cell Death1 (RCD1)-RST interaction motif (RIM) (Christensen et al., 2019). M5 has also been identified in other transcription factor families (Christensen et al., 2019; O'Shea et al., 2017). In clade II-3, M5 is also present in ANAC087 (Christensen et al., 2019). The comparison of the clade C-termini to the AD activity suggests that the presence of acidic and hydrophobic/aromatic residues is needed for activity.

To analyze the interplay between SLiMs, ADs, and contexts within a long IDR, we focused on ANAC046. This transcription factor is a strong activator (Hummel et al., 2023) containing two ADs (Figure 1a) and three of the four identified SLiMs (Figure 1), and it is functionally well-characterized (Mahmood et al., 2019; Oda-Yamamizo et al., 2016). From the AD scores, which report on the potential for a sequence region to activate transcription (Morffy et al., 2024), ANAC046 contains an N-terminal and a C-terminal AD spanning 30 and 18 residues, respectively (Figure 1d). The N-terminal AD (AD1) overlaps with M1 and M2 (Figure 1d, lower). The C-terminal AD (AD2) was identified previously (O'Shea et al., 2015) and overlaps with M5, hinting at regulatory effects of this SLiM in activation. Based on these qualities, we proceeded to provide a detailed molecular characterization of the features of the ANAC046 IDR responsible for coregulator binding.

2.3 | The ANAC046 IDR: Lack of residual structure, with propensity to phase separate

The IDR of ANAC046 spans 167 residues ($ANAC046_{172–338}$) of a 339 residues-long protein (Figure 2a). To characterize the IDR, we first used nuclear magnetic resonance (NMR) spectroscopy. The derived NMR secondary chemical shifts (SCS) of C^{α} and C^{β} nuclei calculated from previous work (Newcombe et al., 2021) showed no consecutive positive and negative values corresponding to secondary structure features (Figures 2b and S4a). From ^{15}N transverse (R_2) and longitudinal (R_1) relaxation rates and $\{^1H\}$-^{15}N heteronuclear NOE (hetNOE) measurements, the backbone dynamics supported the lack of secondary structure but revealed a small increase in R_2 and hetNOE values for parts of both AD1 and AD2 (Figures 2b, c and S4a). Being void of substantial residual secondary structure, AD1 and AD2 may form long-range contacts within the ensemble leading to the observed local increase in R_2.

To address if other features of the sequence of $ANAC046_{172–338}$ would be responsible for the increased R_2-values, we investigated the sequence using IDDomainspotter (Millard et al., 2020) (Figure 2c). This revealed it to be overall hydrophobic with a high content of acidic residues (mainly aspartates) in the two ADs. This agrees with the classification of the two ADs as subtype 1 ADs, which are enriched in these residue types (Morffy et al., 2024). The IDR is rich in aromatic (7% FYW), glycine (8%) and serine (13%) residues, features that have been found in several phase-separating proteins. Consequently, two central regions were predicted to be phase separation-prone (Ibrahim et al., 2023) (Figure 2d), although the full $ANAC046_{172–338}$ sequence is not predicted to

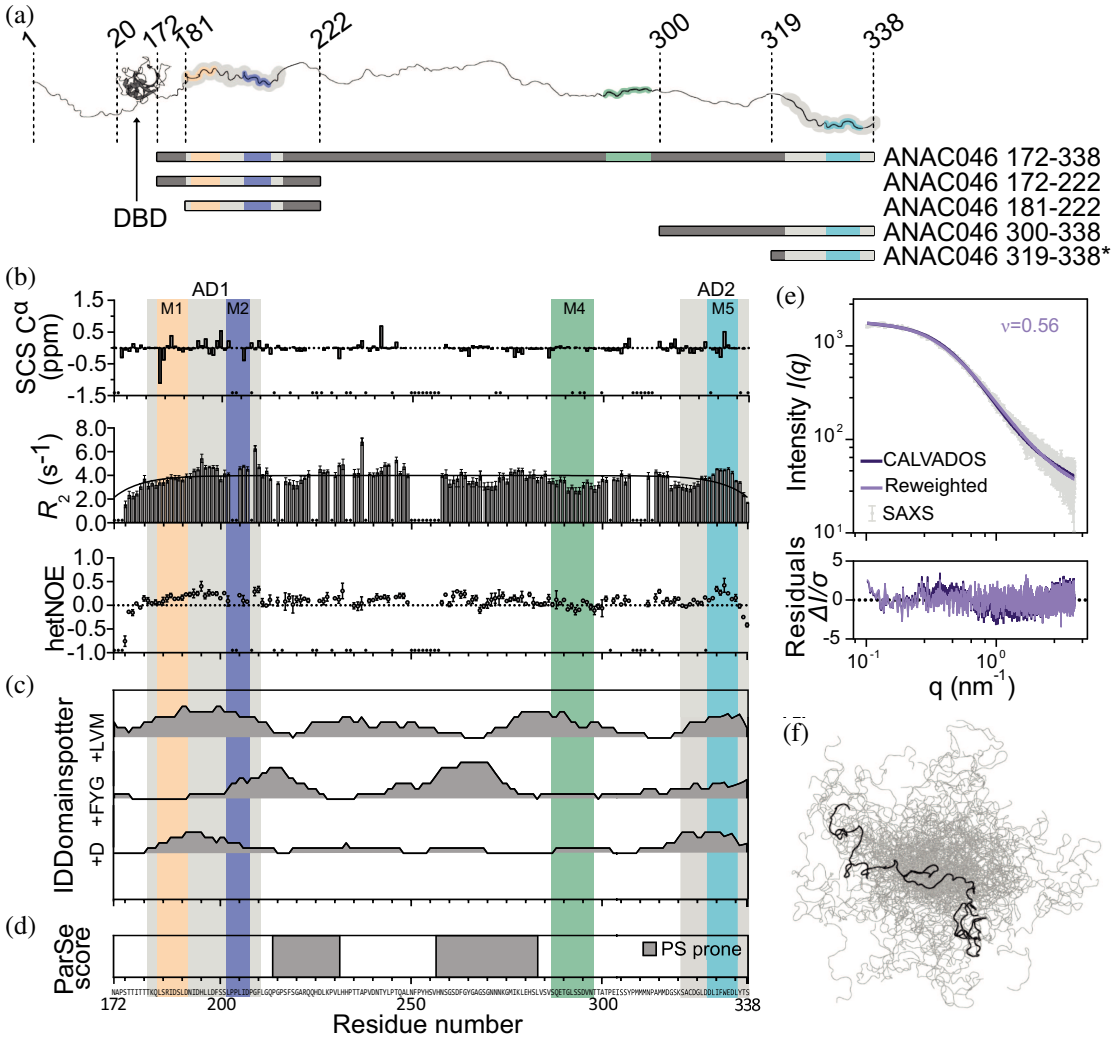

FIGURE 2 The ANAC046 IDR is disordered without residual structure. (a) Domain structure of ANAC046 with fragments used in this work and with an AlphaFold 2 structure in an extended version illustrated above. The fragment noted * is from previous work (O'Shea et al., 2015). (b) C^{α} SCS calculated from Newcombe et al. (2021) (top), R_2 relaxation rates including values for a 167-residue random coil protein shown as a line (Wirmer et al., 2006) (middle) and hetNOEs (bottom) of $ANAC046_{172–338}$. (c) IDDomainspotter (Millard et al., 2020) analysis of $ANAC046_{172–338}$ with a sliding window of 15 residues. (d) ParSe (Wilson et al., 2023) prediction of $ANAC046_{172–338}$ with Identified regions of 20 or more contiguous residues at least 90% PS prone. For (a)–(d), the coloring of the IDR is defined in Figure 1. (e) Double log plot of the experimental SAXS scattering curve of $ANAC046_{172–338}$ (light gray) and calculated SAXS scattering curves from the ensemble generated using CALVADOS 2 (Tesei & Lindorff-Larsen, 2023) before ($\chi^2 = 1.32$) (dark purple) and after ($\chi^2 = 1.00$) (light purple) reweighting. Residuals are shown below. The scaling exponent (ν) is shown in the plot. (f) 50 models sampled randomly from the simulation ensemble with weights from reweighting with one model highlighted.

undergo homotypic phase separation using a recently described sequence-based prediction model (von Bülow et al., 2024).

So far, the characterization of $ANAC046_{172–338}$ suggests a highly dynamic IDR with no residual secondary structure. To address the chain compactness, we recorded small-angle x-ray scattering (SAXS) on $ANAC046_{172–338}$. We also simulated the IDR ensemble using the CALVADOS 2 coarse-grained model (Tesei & Lindorff-Larsen, 2023), and reweighted the ensemble with the SAXS data (Figure 2e, f). From this, we calculated an apparent scaling exponent (ν) of 0.56, in good agreement with a value of 0.53 predicted directly from sequence (Tesei et al., 2024). Compared to the distribution of values of ν found for a broad range of human IDPs (Tesei et al., 2024; Tesei & Lindorff-Larsen, 2023), we find that the ANAC046 IDR ensemble is slightly expanded.

2.4 | The ANAC046 IDR binds regulators promiscuously at overlapping sites

We next explored if the identified AD/SLiM regions, AD1(181–210)/M1(184–191)-M2(202–207) (named AD1/M1-2) and AD2(321–338)/M5(328–297) (named

TABLE 1 Regulator domains analyzed for interactions with ANAC046 AD1/M1-2 and AD2/M5.

Domain	*Arabidopsis* parent protein	Relevance	References
RST	RCD1: negative regulator	Binds transcription factors through M5	(O'Shea et al., 2015; O'Shea et al., 2017; Shapiguzov et al., 2019)
RST	TAF4: coactivator as part of the TFIID transcription initiation TFIID complex	Binds transcription factors through M5	(Friis Theisen et al., 2022)
TAZ1	HAC1: coactivator homolog of human CBP	M2 is similar to TAZ1-binding SLiM LP(Q/E)L	(Berlow et al., 2017)
TAZ2	HAC1: coactivator homolog of human CBP	CBP-TAZ2 binds transcription factors promiscuously	(DelRosso et al., 2024)
KIX	HAC1: coactivator homolog of human CBP	CBP-KIX binds transcription factors specifically	(DelRosso et al., 2024)
ACID	MED25: subunit 25 of the transcriptional coactivator MEDIATOR	MED25-ACID binds various transcription factors	(Theisen et al., 2024)

AD2/M5) in the ANAC046 IDR (Figure 2b), are involved in partner binding. Here, we sought proteins related to both positive and negative regulation (Table 1). We selected the RST domain from the negative regulator RCD1, known for interactions with transcription factors containing M5 (O'Shea et al., 2015; O'Shea et al., 2017; Shapiguzov et al., 2019), and from the positive coregulator TATA-box binding protein associated factor 4 (TAF4). Due to similarities between M2 and the SLiM (LP(Q/E)L), known to bind the TAZ1 domain of CBP (Berlow et al., 2017), we selected the *Arabidopsis* homolog of CBP HAC1 and its KIX, TAZ1, and TAZ2 domains. Lastly, we included the ACID domain of the *Arabidopsis* MEDIATOR subunit 25 (MED25) known to bind transcription factors (Theisen et al., 2024). Overall, a total of six domains from important transcriptional regulators were selected (Table 1); all with a high isoelectric point (pI: 8.7–10.3) and α-helical structures, except MED25-ACID, which forms a β-barrel (Figure S5) (Theisen et al., 2024).

To test whether the regulator domains interact with the ANAC046 IDR, we recorded ^{15}N-HSQC NMR spectra of ^{15}N-ANAC046$_{172–338}$ alone and in the presence of each domain (Figure 3a, b). For all six domains, their presence resulted in a decrease in NMR peak intensities for ANAC046$_{172–338}$ suggestive of interactions. For the HAC1-TAZ2 interaction, a general decrease in peak intensity for signals across the IDR was observed, leaving most peaks almost invisible, mostly in the regions of AD1/M1-2 and AD2/M5 (Figure 3b, annotated peaks). The general signal loss across the chain can be explained by precipitation upon mixing the proteins and happened also to varying degrees for the other domains. To distinguish between the effects from adding the different partners, we focused on the chemical shifts of three residues positioned differently in ANAC046$_{172–338}$: S189 in AD1/M1-2, S261 in the middle part, and M315 near AD2/M5 (Figure 3c). For S261, no change in peak position was observed with any of the partners, suggesting that the central region does not participate in the interactions. S189 and M315, positioned in AD1/M1-2 and at the border of AD2/M5, respectively, experienced different chemical shift perturbations (CSPs) depending on the interacting domain. HAC1-TAZ1, HAC1-KIX, and RCD1-RST induced similar changes for the two residues. Conversely, the spectral changes were similar for the binding of MED25-ACID and TAF4-RST, although S189 did not move in the case of MED25-ACID. Thus, the IDR experienced similar chemical environments for interactions with HAC1-KIX, HAC1-TAZ1, and RCD1-RST, and a different one when interacting with MED25-ACID and TAF4-RST.

To define the regulator binding sites in the ANAC046 IDR, we focused on the systems with the least visible aggregation and performed NMR titrations of ^{15}N-ANAC046$_{172–338}$ with RCD1-RST and HAC1-TAZ1 (Figure 3d, e). Adding RCD1-RST to ^{15}N-ANAC046$_{172–338}$ decreased the intensities of residues within AD1/M1-2 and AD2/M5, the latter with effects exceeding AD2/M5 by covering residues 300–338. The titration with HAC1-TAZ1 was slightly affected by precipitation (Figure 3e). Still, we observed binding of HAC1-TAZ1 to AD1/M1-2 and AD2/M5 including their contexts, highly analogous to the titration with RCD1-RST. Furthermore, changes in the intensities of residues bordering an NMR invisible central region in the IDR (Figure 3d, e, marked with *) could suggest a potential weak third binding site or an induced contact redistribution from partner binding. For the interactions with RCD1-RST and HAC1-TAZ1, where a full titration could be obtained, we note that AD1/M1-2 is in fast to intermediate exchange and AD2/M5 is in intermediate to slow exchange on the NMR time scale (Figure 3c). Due to pronounced precipitation, a full titration of the remaining complexes was not possible. Instead, we analyzed the NMR peak intensity ratios from the spectra in Figure 3a (I_{bound}/I_{free}) except for the HAC1-TAZ2 complex, due to extensive precipitation (Figure S11). From these ratios, it is evident that all five domains bind

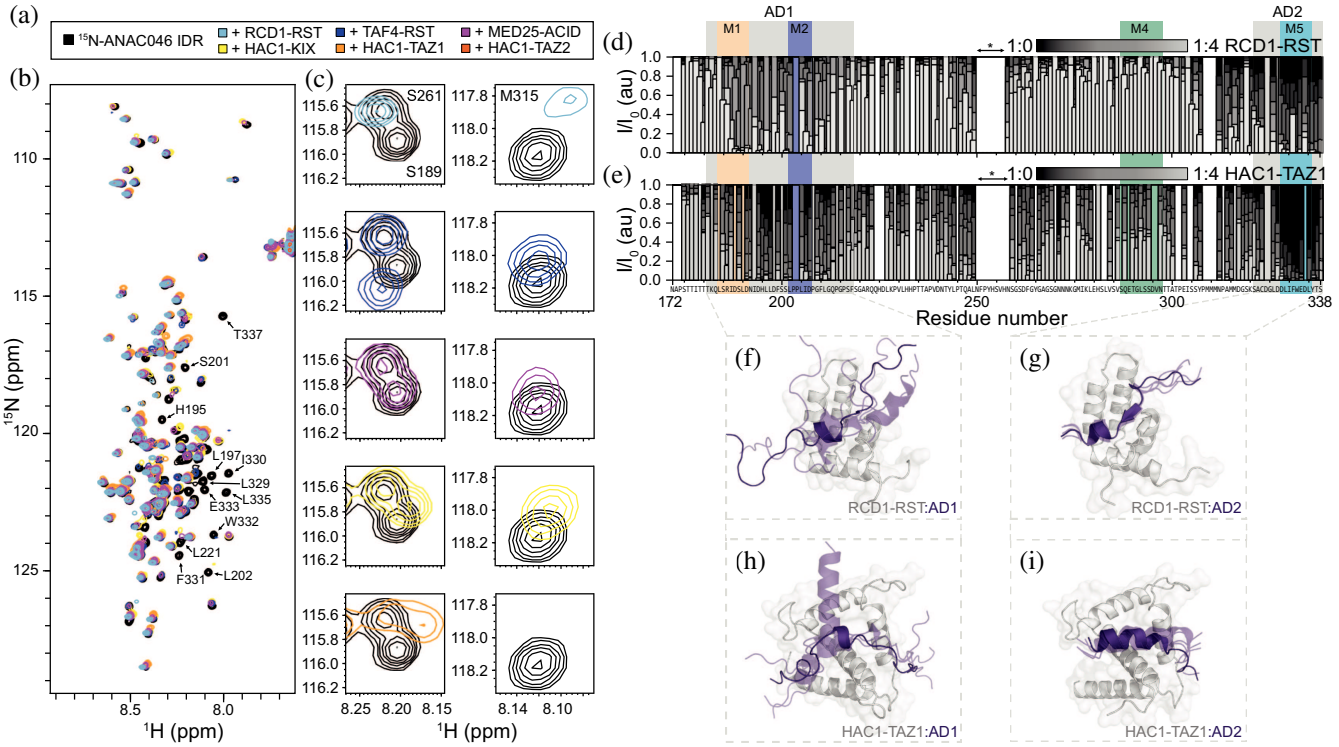

FIGURE 3 Regulator binding to ANAC046 IDR is promiscuous at specific sites. (a) Overview of proteins used for analyses with colors used in (b) and (c). (b) ^{15}N-HSQCs of ^{15}N-ANAC046$_{172–338}$ with and without (black) added partner. Residues that disappear upon regulator addition are annotated. (c) Zooms on S189 and S261 (left), and M315 (right) in ANAC046$_{172–338}$ in the absence (black) and presence of regulators (for colors see A). (d) and (e) NMR peak intensity ratios (I/I_0) of ^{15}N-ANAC046$_{172–338}$ determined from titration with RCD1-RST (h) and HAC1-TAZ1 (i), respectively. Titration points vary from no addition of regulator to four molar excesses. The SLiMs and ADs identified in the ANAC046 IDR are highlighted. Gaps in the plot show unassigned residues, and residues in the area marked with * were not observed. (f)–(i) AlphaFold 3 models of the two ADs in complex with RCD1-RST and HAC1-TAZ1. The highest-ranking peptide model is shown in purple with other models transparent.

ANAC046 IDR at the same two sites. Based on these NMR observations, the three SLiMs, M1, M2, and M5, are involved in regulator binding, although not alone. The full ADs along with additional flanking regions outside the ADs are also involved in the interactions.

We modeled the complexes between the AD/SLiMs and the different regulator domains using AlphaFold 3 (Abramson et al., 2024) (Figures 3f, i and S6). The models predict in all cases induction of structure in the AD/SLiMs but to various degrees, and with more heterogeneity in the AD1/M1-2 complexes. Thus, for AD2/M5, which exchanges on the intermediate to slow NMR timescale, the models are less heterogeneous, suggesting that the consistency of the AlphaFold 3 models may reflect on the exchange rate and likely the affinity. The recently identified core structure formed by transcription factors in complexes with RCD1-RST consisting of a short strand followed by a turn (Newcombe et al., 2024), is only present in the RCD1-RST:AD2/M5 complex (Figure 3g). However, the turn is formed in both AD1/M1-2 and AD2/M5 in complex with RCD1-RST and TAF4-RST. In these two complexes, AD1/M1-2 and AD2/M5 share the RST-binding site, although in the TAF4-RST:AD2/M5 models, the AD2/M5 orientation is reversed compared to that in RCD1-RST:AD2/M5. For AD1/M1-2, the orientations vary for the different models with RCD1-RST, whereas there is only one orientation of AD1/M1-2 in complex with TAF4-RST (Figures 3f, g and S6). Given the relations observed above regarding exchange regimes and model homogeneity, we speculate that the affinity of AD1/M1-2 for TAF4-RST and HAC1-KIX is higher than for RCD1-RST (Figure S6). In interactions with HAC1-TAZ2 and MED25-ACID, AD1/M1-2 and AD2/M5 use different binding interfaces and are more heterogeneous, potentially alluding to weaker affinities for both (Figure 3h, i and S6). Together with the CSPs, the models suggest that the two AD/SLiMs of ANAC046 bind the same regulators, but with different binding modes and affinities, and with more structural heterogeneity in the AD1/M1-2 complexes.

We determined the affinities of ANAC046-IDR for RCD1-RST and HAC1-TAZ1 using isothermal titration calorimetry (ITC) (Table 2, Figures S7 and S8). A short ANAC046 fragment covering just AD2/M5 (ANAC046$_{319–338}$) was previously reported to bind RCD1-RST with a K_D of 0.6 μM (O'Shea et al., 2015). However, with the expanded binding region identified from NMR, we designed a longer fragment covering the region 300–338 (ANAC046$_{300–338}$). For

TABLE 2 Thermodynamic parameters of interactions between ANAC046 and regulators.

Cell/syringe	*N*	K_D (μM)	Δ*H* (kJ/mol)	−*T*Δ*S* (kJ/mol)	Δ*G* (kJ/mol)
RCD1-RST$_{499–572}$/ANAC046$_{319–338}$[a]	0.88 ± 0.04	0.6 ± 0.1	−24 ± 1	−11.3	−35.1
RCD1-RST$_{499–572}$/ANAC046$_{172–222}$[b]	-	148 ± 6	-	-	-
RCD1-RST$_{499–572}$/ANAC046$_{300–338}$	0.8 ± 0.1	0.12 ± 0.05	−31 ± 7	−8 ± 8	−40 ± 1
ANAC046$_{172–338}$ /RCD1-RST$_{499–572}$	0.89 ± 0.08	0.20 ± 0.07	−23 ± 2	−15 ± 3	−38.5 ± 0.8
HAC1-TAZ1/ANAC046$_{172–222}$[b]	-	112 ± 6	-	-	-
ANAC046$_{300–338}$/HAC1-TAZ1	0.97 ± 0.09	6 ± 2	−25 ± 1	−5 ± 2	−29.9 ± 0.7
ANAC046$_{172–338}$/ HAC1-TAZ1[c]	0.91 ± 0.01	3.0 ± 0.3	−25 ± 2	−7 ± 2	−31.5 ± 0.2
	1.12 ± 0.03	260 ± 10	−65 ± 4	44 ± 4	−20.5 ± 0.1

Note: Error on ITC obtained in this study is given as SEM from triplicates.
[a]From O'Shea et al. (2015).
[b]Interaction not measurable by ITC, affinity obtained from NMR including error of fit.
[c]The interaction was fitted to a two-site binding model corresponding to two sets of sites.

ANAC046$_{300–338}$, a K_D of 0.12 ± 0.05 μM was obtained, increasing the affinity five-fold compared to the shorter ANAC046$_{319–338}$. The enhanced binding is reflected in an increased binding enthalpy (more negative Δ*H*) highlighting context contribution to M5 binding/core structure formation. The same ANAC046 fragment had a 50-fold lower affinity for HAC1-TAZ1 ($K_D = 6 \pm 2$ μM). Due to unfavorable injection heats, the binding of a fragment containing AD1/M1-2 (ANAC046$_{172–222}$) to the two regulators could not be analyzed by ITC. Instead, we used NMR and determined similar K_D values of 148 ± 6 μM and 112 ± 6 μM for the binding to RCD1-RST and HAC1-TAZ1, respectively (Table 2, Figures S9 and S10). Thus, there is a hierarchy in binding, with AD2/M5 binding the regulators more strongly than AD1/M1-2. Based on the linker length between AD1/M1-2 and AD2/M5 (110 residues), we did not expect avidity or allovalency effects (Olsen et al., 2017) within the full IDR (ANAC046$_{172–338}$) and ITC only captured the high-affinity site (AD2) for binding ANAC046$_{172–338}$ to RCD1-RST. For the interaction with HAC1-TAZ1, we were able to probe the interactions of both AD/SLiMs to ANAC046$_{172–338}$ using ITC, resulting in K_D values of 260 ± 10 μM and 3.0 ± 0.3 μM for AD1/M1-2 and AD2/M5, respectively, and with highly unfavorable entropic effects for AD1/M1-2 (Figure 4a). This was in accordance with the affinities obtained with the individual AD/SLiMs alone (ANAC046$_{172–222}$ and ANAC046$_{300–338}$), underscoring the lack of coupling between AD1/M1-2 and AD2/M5 in regulator binding. For both regulators, two binding sites within the long IDR were observed ($n = 2$).

The thermodynamic analysis revealed a favorable entropic contribution to the interactions of regulator domains and AD/SLiMs in the ANAC046 IDR, except for the association between AD1/M1-2 and HAC1-TAZ1 (Figure 4a). The favorable entropic contribution suggests a dynamic interaction sustained by conformational entropy (Skriver et al., 2023), consistent with the AlphaFold 3 models, although contributions from water and counterion release could also contribute. Dynamics in this complex agree with a recent study showing that substituting the normal L-amino acid version of AD2/M5 with the D-version had little effect on ANAC046 binding (Newcombe et al., 2024). From the experiments with ANAC046$_{172–338}$ and HAC1-TAZ1, the entropic penalty of the AD1/M1-2 association with HAC1-TAZ1 may suggest conformational restrictions upon complex formation involving the long ANAC046 IDR (Figure 4a). However, due to the aggregation impeding high-concentration analyses, the interpretation of the thermodynamics for AD1/M1-2 should be done with caution. Overall, the entropic contribution suggests a dynamic interaction between the AD/SLiMs of the ANAC046 IDR and the regulator domains.

2.5 | Intramolecular interactions in the ANAC046 IDR

To explain the decrease in peak intensity in the central ANAC046 IDR region upon the addition of RCD1-RST or HAC1-TAZ1, which could not be explained by a third binding site, we analyzed the ANAC046 IDR for internal contacts. We explored three positions, S217C in AD1/M1-2, S259C central in the IDR, and C323 in AD2/M5. These sites were selected to be located close to, but outside, the two AD/SLiM regions and the NMR-invisible central region. We added S-(1-oxyl-2,-2,5,5-tetramethyl-2,5-dihydro-1H-pyrrol-3-yl)methyl-methanesulfonothioate (MTSL) as a spin label for measuring paramagnetic relaxation enhancements (PREs) using NMR. This allows detection of long-range (up to 2.5 nm (Sjodt & Clubb, 2017)) distances by the unpaired electron. A control experiment adding MTSL-labeled ^{14}N-ANAC046$_{172–338}$ to ^{15}N-ANAC046$_{172–338}$ did not show any intermolecular effects (Figure S12), ruling out oligomerization. Thus, any effects of the MTSL label were dominantly caused by intrachain contacts. HSQCs of ANAC046$_{172–338}$ with the label in

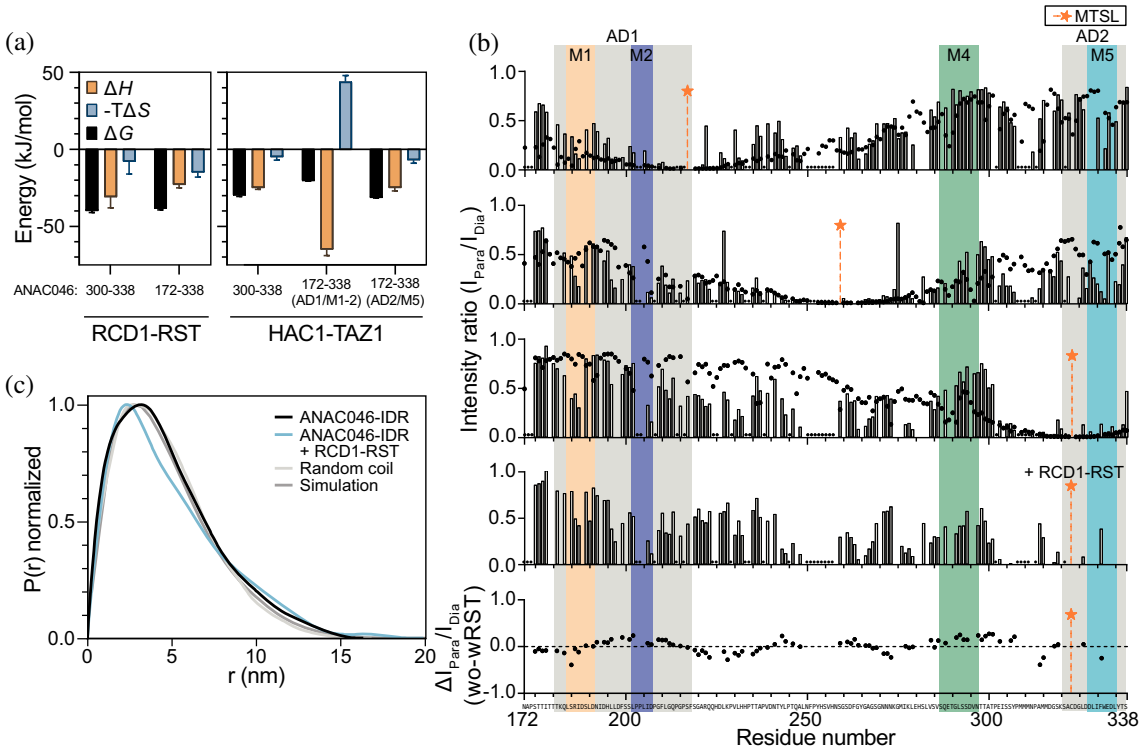

FIGURE 4 Thermodynamics and intramolecular contacts in ANAC046 IDR. (a) Bar plots of the thermodynamic parameters from ITC with different ANAC046 fragments and regulator domains. (b) The three top panels show PRE-NMR with positions labeled by MTSL shown as orange stars at S217C, S259C, and C323. The two lower panels show PRE-NMR with ANAC046-C323 MTSL labeled and added RCD1-RST(1:1 stoichiometric ratio), and the difference PRE between ANAC046-C323-MTSL and ANAC046-C323-MTSL:RCD1-RST (wo-w(RCD1-RST)). For each sample, 90 μM ^{15}N-ANAC046$_{172–338}$ was used and best-TROSY HSQCs recorded in the paramagnetic and diamagnetic states (+ascorbic acid) of the label. The intensity ratios (I_{Para}/I_{Dia}) are plotted for each residue. *unassigned residues. Gaps correspond to ambiguous assignments due to peak overlap. For the top three panels, black dots represent PREs extracted from the simulated ensemble reweighted with SAXS. (c) Normalized pair distance distribution function of the experimental SAXS data of ANAC046-IDR alone (ANAC046) and at 1:1 molar ratio with RCD1-RST (ANAC046 + RCD1-RST), a random coil ensemble of ANAC046-IDR generated by RANCH (Bernadó et al., 2007) (Random coil) and the simulated ensemble of ANAC046 IDR reweighted with SAXS (Simulation).

paramagnetic and diamagnetic states, respectively, were recorded and peak intensity ratios between the two states calculated (Figure 4b). PRE-effects were observed to different extents throughout the IDR for all label positions, suggesting that the region of the label position contacts the rest of the IDR (Figure 4b). While spin labels at positions 217 or 323 affected intensity ratios mostly in AD1/M1-2 and AD2/M5 and in the central part of the IDR, a spin label at position 259 showed PREs throughout the IDR (Figure 4b).

The internal contacts revealed by the PREs made us revisit the reweighted IDR ensemble (Figure 2e) to address whether the ensemble could explain the PRE data (Tesei, Martins, et al., 2021). We derived the PRE effects from the simulated ensemble reweighted with SAXS, and overall, there was good agreement between the results obtained from the ensemble-derived and experimental approaches (Figure 4b, black dots), in particular for the PREs measured with labels at positions 217 and 259. This shows that the ANAC046-IDR can form dynamic internal contacts along the IDR and that long-range contacts (>8 Å) are more frequent than in a random coil chain as evident from the pair-distance distribution plots (Figure 4c). Together, this highlights the extensive dynamic molecular communication within the ANAC046-IDR ensemble, facilitated by long-range contacts.

We finally addressed whether the contact distribution within the ANAC046 IDR would be altered upon regulator interaction. Here, we exploited position 323 and added a 1:1 molar ratio of RCD1-RST to ^{15}N-ANAC046$_{172–338}$ C323-MTSL, which at the concentration used primarily saturates AD2/M5 (96%) and to a lesser degree AD1/M1-2 (2%) (Figure 4b, last panel). Increased PRE effects induced by RCD1-RST binding compared to unbound ANAC046-IDR were seen throughout the IDR, suggesting that RCD1-RST further stabilizes the internal contacts in ANAC046 (Figure 4b, lower panel). Supporting this conclusion, SAXS data revealed an R_g for the ANAC046 IDR alone of 3.53 ± 0.03 nm and 3.80 ± 0.04 nm in complex with RCD1-RST (in a 1:1 ratio complex) (Figure S13), and with an increased proportion of long-range distances (>8 Å) in the ensemble (Figure 4c). Overall, this

supports the conclusion that the ANAC046 IDR retains its intramolecular interactions when bound to a partner.

3 | DISCUSSION

In this work, we analyzed if SLiMs and ADs may coincide in long IDRs of transcription factors. Our SLiM search of the NAC II-3 clade resulted in the identification of M1-M4, with instances in additional *Arabidopsis* transcription factors for all but M3. Their functions remain unknown, and the importance of SLiMs for AD function is still debated (Udupa et al., 2024). A fifth SLiM, M5, was functionally identified in the C-terminal regions of the proteins in the clade. Although M1, M2, and M5 overlap with ADs in two regulatory hotspots in ANAC046 and ANAC087, SLiMs and ADs do not consistently overlap in the members of clade II-3. However, not all ADs may be identified in this specific screen (Morffy et al., 2024), in part explaining the lack of systematic overlap between SLiMs and ADs.

We paid special attention to ANAC046, carrying two distant AD/SLiM regions separated by a long linker region, and representing a suitable model for studies of the molecular ensemble characteristics of and functional interplay in a long transcription factor IDR. The ANAC046 IDR lacks residual secondary structure and populates an ensemble with the potential for dynamic molecular communication through long-range contacts. Although the central part of the IDR facilitates most of the contacts, the AD/SLiM regions at each end of the ANAC046 IDR also transiently interact. The ensemble distribution and compactness can affect the transcriptional activity of transcription factors (Flores et al., 2024). From the SAXS data, regulator binding to the C-terminal AD/SLiM does not change the overall ensemble size; in fact, it may slightly increase the number of long-range contacts. At higher regulator concentrations, where both AD/SLiM regions would be occupied, compaction may, however, change.

The two regulatory hotspots in the ANAC046 IDR are separated by a long linker, and we asked what features this could carry. First, the long flexible linker may provide conformational buffering (González-Foutel et al., 2022). Second, the linker possesses features such as phase separation propensity and a long SLiM (M4) of potential additional functional importance. NMR titrations of ANAC046$_{172–338}$ with the different regulator domains resulted in a general peak intensity decrease across the IDR, likely due to precipitation upon mixing. This suggests that the ANAC046 IDR may undergo aggregation and even condensate formation in the presence of regulators (Figure 5a) as in the case of *Arabidopsis* HAC and transcription factors (Theisen et al., 2024). For M4, its length suggests that it can be divided into two SLiMs, one of which resembles a (S/T) Q motif phosphorylated by stress kinases (Kim et al., 1999). From the PRE analysis, the M4 region is devoid of intramolecular communication at least in the absence of phosphorylation. Thus, phosphorylation of

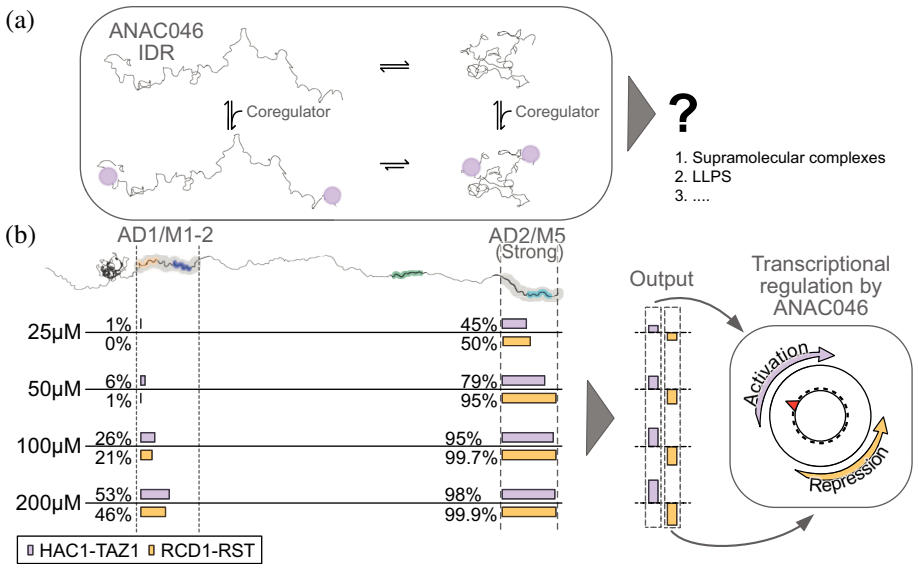

FIGURE 5 Rheostatic regulator binding model of ANAC046. (a) Perturbation in ensemble dynamics of the ANAC046 IDR can lead to the formation of large clusters, supramolecular complexes, or phase separation, also induced by regulator interactions. (b) (Left) For four different regulator domain concentrations and an ANAC046 concentration of 50 μM, site saturation was calculated (Wang, 1995) using the K_d values for AD1/M1-2 (ANAC046$_{172-222}$) and AD2/M5 (ANAC046$_{300-338}$) in the full-length ANAC046 IDR. (Right) The overall saturation of the two AD/SLiMs at different regulator concentrations (output) depends on differences in affinities with a preference for AD2/M5. Depending on the relative levels of positive and negative regulators, we suggest a model with a graded regulator response depending on concentrations and affinities, illustrated as a dial.

this region may play a regulatory role in the ANAC046 IDR ensemble redistribution.

Generally, ADs are regarded as functionally interchangeable (Ptashne & Gann, 1997) and able to bind unrelated regulators (Ravarani et al., 2018; Sigler, 1988; Warfield et al., 2014). Here, we analyzed the binding of the AD/SLiM hotspot regions of ANAC046 to a set of six biologically relevant regulator domains. Indeed, both AD1, overlapping with M1 and M2, and AD2, overlapping with M5, were able to bind all these domains. This seemingly low specificity contrasts with results from recent studies of human CBP showing that the KIX domain binds specific ADs, while the TAZ2 domain is promiscuous in its binding mode, interacting with many ADs (DelRosso et al., 2024). Our approach allowed us to ask what happens to the structure-less AD/SLiM regions of ANAC046 upon complex formation. Our recent work revealed that transcription factors from different transcription factor families share a core structure in complex with RCD1-RST (Newcombe et al., 2024). The AlphaFold 3 models of AD1/M1-2 and AD2/M5 in complex with the different regulatory domains reveal a complete core structure only in the interaction between RCD1-RST and AD/SLiMs, while the turn of the core structure may form in other complexes. In additional models, the AD/SLiMs of ANAC046 all form turn or helical structure to varying degrees and mostly bind to different binding surfaces, with larger heterogeneity in the AD1/M1-2 complexes. Together with the entropic contribution determined by ITC, this suggests that the complexes between AD/SLiMs and regulator domains are dynamic, as suggested for the RCD1-RST:AD2/M5 interaction (Newcombe et al., 2024). Understanding specificities in these types of interactions is complicated by their dynamics and heterogeneity. Limited chemical specificity of the ANAC046 hotspots can lead to a broad range of interactions that are context-dependent and influenced by the cellular environment.

Based on our studies, AD2/M5 binds with higher affinity than AD1/M1-2 to the regulators. This suggests that the binding of regulators confers a graded response to a cellular cue, with an output depending on the competitive binding of positive and negative regulators (Figure 5b). RCD1, binding with the highest affinity to AD2/M5 exposed at the end of a long flexible chain, would first bind here. RCD1-RST may then bind AD1/M1-2 but occupy it only partially due to the lower affinity. A similar sequential binding was observed for HAC1-TAZ1 binding to the two ANAC046 AD/SLiMs. Thus, due to the differences in K_d values, the regulation of ANAC046 appears to be both hierarchical and rheostatic. This further implies that regulators with a large difference in K_d values between the two AD/SLiM sites would be operational over a wider concentration range. This will facilitate a broader dynamic response window, regulation enabled by the presence of more than one AD/SLiM region. Together, this suggests a promiscuous binding strategy within the IDR of ANAC046 functioning in competition-based rheostatic regulation with little chemical specificity but relying on the protein levels of both positive and negative regulators, regulated by, for example, stress and senescence as in the case of ANAC046 (Oda-Yamamizo et al., 2016) or by modifications. The existence of two distant and uncoupled AD/SLiMs explains how ANAC046 is a strong activator (Hummel et al., 2023) with the ability to fine-tune transcription. We suggest that similar regulation mechanisms are mirrored in other transcription factors with AD-dependent regulation through distant AD/SLiM regions.

4 | MATERIALS AND METHODS

4.1 | Bioinformatics

The *viridiplantae* ortholog alignments from Proviz (Jehl et al., 2016) were exported for each of the C-terminal IDRs of the clade II-3 transcription factors; a logo plot was constructed in a logo generator (http://slim.icr.ac.uk/visualisation/) using the relative binomial representation.

Conserved regions in a non-conserved context that followed the definition of a SLIM (approximately 4–10 residues in length) and found in multiple IDR logos were identified and extracted. To identify instances in other *Arabidopsis* transcription factors, sequence alignments were generated for SLiM-containing regions from transcription factor orthologs using GOPHER (Davey et al., 2007) in other *viridiplantae* species. Each sequence in the alignments was scored against the original *Arabidopsis* query SLiM regions using BLOSUM62, and peptide sequences with a score of less than 75% were discarded. The sequence alignments for the remaining sequences were used to generate position-specific scoring matrix (PSSM) in PSSMSearch (Krystkowiak et al., 2018) for each SLiM. The PSI-blast IC scoring method with default settings was used for searching the *Arabidopsis* proteome. The instance list was filtered based on *Arabidopsis* transcription factors in PlantTFDB (Jin et al., 2017), on disorder scores (IUPred (Erdős et al., 2021) score >0.4), and on accessibility (pLDDT score >0.5). For each SLiM, the residue frequency at each position in the PSSM (Figure S2) was used to define a SLiM consensus. Two SLiM consensus sequences were identified for M4, resulting in individual filtering analyses.

Sequence properties and residue-type density in the transcription factor IDRs were illustrated using IDDomainspotter applying default settings (Millard et al., 2020). To analyze the ANAC046$_{172–338}$ sequence for propensities for phase separation ParSe (Ibrahim et al., 2023) was used with default settings.

The C-termini (21 residues) of the NAC clade were analyzed using Clustal Omega (Sievers & Higgins, 2018).

4.2 | Protein expression and purification

The IDR of ANAC046 ($ANAC046_{172–338}$) was expressed in the pET24a vector in Rosetta (DE3) and purified with a His_6-SUMO tag either as previously described (Newcombe et al., 2021) or as detailed below. The cells were lysed by sonication in 20 mM Na_2HPO_4/NaH_2PO_4 pH 7.0, 300 mM NaCl (also used as equilibration buffer and wash buffer) on ice and centrifuged at 18.000 rpm for 15 min at 4°C. The lysate was purified using immobilized metal affinity chromatography (IMAC) with TALON® Superflow™ (Cytiva) resin (5 mL pr L culture). After equilibration, the resin was incubated with the lysate for 1 h at 4°C under rotation. The resin was washed with wash buffer for 3 column volumes (CV). Bound protein was eluted with 20 mM Na_2HPO_4/NaH_2PO_4 pH 7.0, 100 mM NaCl, and 250 mM imidazole (2 CV). Before cleavage, the sample was dialyzed against 20 mM Na_2HPO_4/NaH_2PO_4, pH 7.0, 100 mM NaCl, 1 mM dithiothreitol (DTT) to remove imidazole. Cleavage of the His_6-SUMO-tag with Ubl-specific protease 1 (ULP1) (produced in-house (Singh & Graether, 2020)) was performed for 3 h on rotation at 4°C. A second IMAC purification step resulted in the protein being in the flow through, which was concentrated using an Amicon® spin filter (MWCO 10 kDa, Millipore), followed by acid precipitation of the IDR (Newcombe et al., 2021). This step was repeated before purification using size exclusion chromatography (SEC) in the desired experimental buffer (Superdex™ Increase 75 10/300 GL, GE Healthcare).

Variants of $ANAC046_{172–338}$ containing cysteine mutations, $ANAC046_{172–338,S259C;C323S}$ and $ANAC046_{172–338,S217C;C323S}$ were expressed with a His_6-SUMO tag using a pET24a vector in BL21 (DE3) and purified as described for $ANAC046_{172–338}$.

$ANAC046_{172–222,S175W}$ and $ANAC046_{300–338}$ were expressed with an N-terminal His_6-SUMO tag using a pET24a vector in BL21 (DE3) cells. The cells grew at 37°C to OD_{600} 0.6–0.8 before induction with 1 mM isopropyl ß-D-1-thiogalactopyranoside (IPTG) and incubated overnight at 16°C.

For $ANAC046_{172–222,S175W}$, cells were lysed in 50 mM Na_2HPO_4/NaH_2PO_4, pH 7.0, 150 mM NaCl by sonication. After centrifugation, the lysate was purified by IMAC (TALON® Superflow™, Cytiva) (5 mL resin pr 1 L culture) equilibrated in lysis buffer. After incubation for 1 h, the resin was washed with 50 mM Na_2HPO_4/NaH_2PO_4, pH 7.0, 300 mM NaCl (10 CV) before elution with 50 mM Na_2HPO_4/NaH_2PO_4, pH 7.0, 150 mM NaCl, 250 mM imidazole (2 CV). The eluate was dialyzed against 50 mM Na_2HPO_4/NaH_2PO_4, pH 7.0, 150 mM NaCl, and the His_6-SUMO-tag was cleaved with ULP1 overnight at 4°C under rotation with 1 mM DTT added to the sample. The sample was further purified using SEC (Superdex™ Peptide 10/300 GL, Cytiva) into the desired experimental buffer. A similar protocol was used for $ANAC046_{300–338}$ with different buffers. 20 mM Tris–HCl pH 8.0, 300 mM NaCl was used under lysis and equilibration and wash steps of the IMAC column. 20 mM Tris–HCl pH 8.0, 100 mM NaCl, 250 mM imidazole was used under IMAC elution. The dialysis buffer was 20 mM Tris–HCl pH 8.0, 100 mM NaCl. After cleavage with ULP1 (same conditions as for $ANAC046_{172–222}$), a second IMAC step was performed as the first. The flowthrough from the second IMAC step was purified using SEC.

The RCD1-RST (residues S499-S572) and TAF4-RST (residues N182-Y254) were expressed and purified as described (Bugge et al., 2018; Friis Theisen et al., 2022). As a final purification step, a SEC was performed using Superdex™ Increase 75 10/300 GL (GE Healthcare). The MED25-ACID (residues S532-N680) was expressed and purified as described by (Theisen et al., 2024).

From HAC1 (UniProt ID: Q9C5X9), the coding sequences of the domains of HAC1-KIX (G43-N134), HAC1-TAZ1 (G626-R724) and HAC1-TAZ2 (N1574-G1697) were selected. HAC1-KIX and HAC1-TAZ2 were expressed with an N-terminal His_6-SUMO tag using a pET24a vector, and the HAC1-TAZ1 domain was expressed without a tag in a pET11a vector, all in BL21 (DE3) cells. All domains were expressed after OD_{600} reached 0.6–0.8 (grown at 37°C), induced with 1 mM IPTG, and incubated overnight at 16°C. A final concentration of 150 μM $ZnSO_4$ for the TAZ domains was added at induction.

Cells expressing HAC1-KIX were lysed by sonication in 20 mM Tris–HCl pH 8.0, 300 mM NaCl. The lysate was purified using IMAC (TALON® Superflow™, Cytiva) with 5 mL resin per L culture equilibrated with 20 mM Tris–HCl pH 8, 300 mM NaCl and incubated for 1 h at 4°C. The resin was washed with equilibration buffer (10 CV) and the protein was eluted in 20 mM Tris–HCl pH 8, 100 mM NaCl, 250 mM imidazole (2 CV). The eluate was dialyzed against 20 mM Tris–HCl pH 8, 100 mM NaCl before cleavage of the His_6-SUMO-tag with ULP1 (0.05 mg) for 2 h at 4°C on rotation. A second IMAC step was performed as just described and the flow-through was dialyzed against 20 mM Tris–HCl pH 8.8, 20 mM NaCl. An ion exchange chromatography (IEX) step with a gradient of 20 mM to 1 M NaCl in 20 mM Tris–HCl pH 8.8 (SOURCE™ 15S, Cytiva, 1 mL/min flow) was performed before SEC (Superdex™ Increase 75 10/300 GL, GE Healthcare).

Cells expressing HAC1-TAZ1 were lysed in 20 mM Tris–HCl pH 8.0, 50 mM NaCl, 10 μM $ZnSO_4$, 1 mM DTT by sonication. The lysate was purified using IEX with a SOURCE™ 15S column (GE Healthcare)

equilibrated with the same buffer as used under cell lysis. The gradient was 50 mM to 1 M NaCl. Fractions containing the domain were further purified using SEC (Superdex™ Increase 75 10/300 GL, GE Healthcare).

Cells expressing HAC1-TAZ2 were lysed by sonication in 20 mM Tris–HCl pH 8.0, 20 mM NaCl, 10 μM $ZnSO_4$, 1 mM DTT. The lysate was purified by IEX (SOURCE™ 15S, Cytiva) with a gradient of 20 mM to 1 M NaCl in 20 mM Tris–HCl pH 8.0, 10 μM $ZnSO_4$, 1 mM DTT. The fractions containing protein were pooled, and a cleavage step was performed by adding 0.05 mg ULP1 to cleave off the His_6-SUMO tag, incubating for 2 h at 4°C under rotation. A second IEX step was performed under similar conditions but at pH 9.0. A final step of SEC (Superdex™ Increase 75 10/300 GL, GE Healthcare).

For S-(1-oxyl-2,2,5,5-tetramethyl-2,5-dihydro-1H-pyrrol-3-yl)methyl methanesulfonothioate (MTSL)-labeling of $ANAC046_{172–338}$ variants, we utilized a single internal cysteine. For the purified proteins, a final concentration of 5 mM fresh DTT was added, incubating for 30 min at 4°C; subsequently, buffer exchanged using a PD10 desalting column (Cytiva) into 50 mM Hepes pH 8.0, 50 mM NaCl, 3 M GdnHCl. The sample was collected in a foil-covered tube, and MTSL was added at a 10× molar excess. The sample was flushed with nitrogen and incubated overnight (at least 16 h) at room temperature under rotation. Separation of the labeled protein from the free label and unlabeled protein was performed using reverse phase chromatography (RPC) (RESOURCE™ RPC, 3 mL (Cytiva)) with a gradient of buffer A (50 mM NH_3HCO_3 in MilliQ) and buffer B (30 mM NH_3HCO_3, 70% acetonitrile).

Protein concentrations were in all cases determined from the absorbance at 280 nm and the extinction coefficients were determined using the ProtParam tool at the ExPASy server using the primary structure of the proteins as input with all cysteines reduced.

4.3 | Small angle x-ray scattering

SAXS data was obtained on the PETRA III P12 beamline (DESY, Hamburg) using batch-mode acquisition at 25°C following standard procedures except the transmission was set to 50%. Primary data reduction was made in BIOXTAS RAW. Recordings on $ANAC046_{172–338}$ were made alone or in a 1:1 complex with RCD1-RST with different concentrations of 0.7, 1.4 mg/mL, and 1 mg/mL complex, respectively, in 20 mM Na_2HPO_4/NaH_2PO_4 pH 7.0, 100 mM NaCl, 5 mM DTT. Using the ATSAS package (Petoukhov et al., 2012), the scattering curves were manually assessed, averaged, and subtracted with averaged buffer scattering curves. The R_gs were extracted from the scattering curves using the ATSAS package for one concentration of each protein condition. The scattering curves of the ANAC046 IDR alone were used to build a coarse-grain model of the IDR ensemble. The RANCH application from the EOM (Bernadó et al., 2007) suite (part of ATSAS) was used to generate 100 random models of $ANAC046_{172–338}$ to produce a scattering curve using the CRYSOL application (ATSAS). Pair-distance distribution functions were generated from scattering curves using the GNOM application in ATSAS.

4.4 | Nuclear magnetic resonance spectroscopy

All NMR experiments were acquired on Bruker AVANCE 600 or 800 MHz (^{1}H) spectrometers equipped with cryogenic probes. All experiments were performed in 20 mM Na_2HPO_4/NaH_2PO_4, pH 7.0, 100 mM NaCl, 1 mM DTT, 10% (v/v) D_2O, 0.02% (w/v) NaN_3, and 0.2 mM 4,4-dimethyl-4-silapentane-1sulfonic acid (DSS) except for HAC1-TAZ1 or -TAZ2; here 20 mM Hepes, pH 7.0 was used in the absence of DSS (a similar sample was made containing DSS without the domains for referencing). Assignments of free $ANAC046_{172–338}$ were from previous work (BMRB ID:51033) (Newcombe et al., 2021). ^{15}N,^{1}H-HSQCs were recorded for samples containing 50 μM ^{15}N-$ANAC046_{172–338}$ alone and with either 200 μM RCD1-RST, 200 μM TAF4-RST, 75 μM MED25-ACID, 200 μM HAC1-TAZ1, 200 μM HAC1-KIX, or 75 μM HAC1-TAZ2, respectively. Titrations of ^{15}N-$ANAC046_{172–338}$ (50 μM) with RCD1-RST and HAC1-TAZ1 were obtained with molar ratios varying from 0.1 to 4 at 10°C. From the titrations, peak intensity ratios were calculated. Titration experiments were also recorded at 25°C on 75 μM ^{15}N-RCD1-RST or 75 μM ^{15}N-HAC1-TAZ1 with $ANAC046_{172–222}$ of varying molar ratios from 0.1 to 5.

CSPs of the amides were calculated for the titration of ^{15}N-RCD1-RST from Equation (1) (Mulder et al., 1999):

$$\mathrm{CSP} = \sqrt{\left(\Delta\delta_{1_H}\right)^2 + \left(0.154 \cdot \Delta\delta_{15_N}\right)^2} \quad (1)$$

The CSPs were fitted to a one-binding-site model using Equation (2) (Teilum et al., 2017):

$$\Delta\delta_{\mathrm{obs}} = \Delta\delta_{\mathrm{max}} \frac{\left([P]_t + [L]_t + K_d\right) - \left(\left([P]_t + [L]_t + K_d\right)^2 - 4[P]_t[L]_t\right)^{\frac{1}{2}}}{2[P]_t} \quad (2)$$

R_2 and R_1 relaxation of ^{15}N-$ANAC046_{172–338}$ were determined at 10°C on an AVANCE 600 (^{1}H)

spectrometer with a cryogenic probe using the pulse sequences hsqct2etf3gpsi3d and hsqct1etf3gpsi3d, respectively. The relaxation delays were 20, 60, 100, 200, 400, 600, 800, and 1200 ms for T_1 and 34, 68, 102, 170, 237, 271, 339, and 407 ms for T_2. The interscan delay was set to 2 s. All delays were recorded in triplicates in a randomized manner. After processing using NMRpipe (Delaglio et al., 1995), the data was analyzed with CcpNmr (Vranken et al., 2005). Peak heights at each relaxation delay were extracted and fitted to a single exponential decay function in Prism to get the relaxation rates. Random-coil R_2 values were calculated from Equation (3) with the intrinsic relaxation rate (R_{int}) set to 0.285 s^{-1} (temperature correction), λ_0 is the persistence length of the polypeptide chain and was set to 7, and N is the total length of the polypeptide (Wirmer et al., 2006):

$$R_2^{\text{rc}}(i) = R_{\text{int}} \sum_{j=1}^{N} e^{\frac{|i-j|}{\lambda_0}}, \quad (3)$$

{^{1}H}-^{15}N hetNOE experiments were recorded on ANAC046-IDR$_{172–338}$ in triplicates and processed individually. The data is reported as the mean with standard error of the comean.

To determine paramagnetic relaxation enhancement effects, best-TROSY experiments on a Bruker AVANCE 600 MHz (^{1}H) spectrometer with a cryogenic probe at 10°C were recorded on samples containing 90 μM MTSL-labeled ^{15}N-ANAC046$_{172–338}$, ^{15}N-ANAC046$_{172–338,S217C;C323S}$ or ^{15}N-ANAC046$_{172–338,S259C;C323S}$, a sample with 90 μM MTSL-labeled ^{15}N-ANAC046$_{172–338}$ and 90 μM RCD1-RST or a sample with 50 μM ^{15}N-ANAC046$_{172–338}$ and 50 μM MTSL-labeled ANAC046$_{172–338}$ (paramagnetic state of the label). The same experiments were recorded after obtaining the diamagnetic state by incubation with 10× molar excess ascorbic acid for 3 h at 20°C. The effects were quantified from the ratio between resonance intensities for the individual residues.

4.5 | Isothermal titration calorimetry

All experiments were performed on a MicroCal™ ITC$_{200}$ (GE Healthcare) instrument at 25°C in triplicates. A buffer containing 50 mM Hepes, pH 7.0, 100 mM NaCl, and 1 mM tris(2-carboxyethyl)phosphine (TCEP) (when cysteines were present) was used for all experiments. Samples were centrifuged at 17.000 × g for 10 min at the experimental temperature before loading into the microcalorimeter. Concentrations varied between 10 and 100 μM in the cell and between 100 and 1000 μM in the syringe aiming at a 1:10 cell:syringe concentration ratio. A total of 19 injections were made, with the first being 0.5 μL followed by 2 μL injections. For the interaction of ANAC046$_{172–338}$ with HAC1-TAZ1, a total of 38 injections were made, with a 0.5 μL injection followed by 1 μL injections. All data was analyzed using in-house scripts fitted to either one set or twosets of sites as documented by Microcal and Origin. The data points from the first injection of each experiment were removed in the fitting.

4.6 | Coarse-grained molecular dynamics simulations

We ran a coarse-grained simulation of the ANAC046 IDR (172–338) with the CALVADOS 2 model (Tesei & Lindorff-Larsen, 2023; Tesei, Schulze, et al., 2021) using HOOMD-blue 2.9.3 (Anderson et al., 2020). The simulation was performed using a Langevin integrator at 298 K with an ionic strength of 100 mM and the partial charge of His side chains set based on pH 7.0, corresponding to the conditions of the SAXS experiments. We used a 2 nm cutoff for the Ashbaugh-Hatch potential and a 4 nm cutoff for the Debye–Hückel potential. The simulation was started from an Archimedean spiral arrangement of the protein chain. We equilibrated the system for 10,000 steps with a 5 fs time step and ran the production simulation for 10 μs with a 10 fs time step. For our final ensemble, we extracted 10,000 evenly spaced frames and reconstructed the all-atom structures using Pulchra 3.06 (Rotkiewicz & Skolnick, 2008).

4.7 | SAXS calculations and Bayesian/maximum entropy reweighting

We calculated SAXS profiles from our ensemble of 10,000 frames using Pepsi-SAXS 3.0 (Grudinin et al., 2017). We fixed the parameters for the contrast of the hydration layer, $\delta\rho = 3.34$ e/nm^3, and the volume of displaced solvent, $r_0/r_m = 1.025$, to avoid overfitting to the experimental SAXS profile (Pesce & Lindorff-Larsen, 2021). We used a Bayesian/maximum entropy (BME) approach to reweight our ensemble against the experimental SAXS data (Bottaro et al., 2020). We iteratively fitted the scale and constant background of the ensemble averaged SAXS profile while reweighting (Pesce & Lindorff-Larsen, 2021). In BME reweighting, the parameter θ is used to tune the balance between the agreement with the prior ensemble and the experimental data. We scanned θ and selected a value that gave a large decrease in the reduced χ^2 (χ^2_r) to the experimental data while remaining as close to the prior ensemble as possible, as measured by the fraction of effective frames (φ_{eff}). Before reweighting, we used the Bayesian Indirect Fourier Transform algorithm (BIFT) to rescale the errors of the experimental SAXS intensities

to make $\chi^2_r = 1$ the target value for our ensemble model (Hansen, 2000; Larsen & Pedersen, 2021).

4.8 | Scaling exponent calculation

The scaling exponent, ν, was determined using a least-squares fit of the function $r_{ij} = r_0|i-j|^{\nu}$ in the long-distance region $|i-j| > 10$ with r_0 and ν as free parameters, where r_{ij} is the ensemble averaged distance between residues i and j in the sequence and r_0 is a prefactor related to the length of a residue. We used the compute distances function in MDTraj (McGibbon et al., 2015) to calculate r_{ij} and the curve fit function in SciPy (Virtanen et al., 2020) for least-squares regression.

4.9 | PRE calculations from ensemble

We used a rotamer library approach implemented in the DEER-PREdict software (Tesei, Martins, et al., 2021) to calculate PREs from our ensemble, both with uniform weights and with weights from BME reweighting against SAXS. We assumed an effective correlation time of the spin label (τ_t) of 100 ps, a transverse relaxation rate for the diamagnetic protein of 10 $s,^{-1}$ and a total INEPT time of the HSQC measurement of 5.4 ms. We scanned values of the rotational correlation time (τ_c) from 1 to 20 ns in steps of 1 ns and selected 12 ns as the value that minimized the χ^2_r to the experimental PRE data for both the uniform and reweighted ensemble.

AUTHOR CONTRIBUTIONS

Amanda D. Due: Conceptualization; investigation; formal analysis; visualization; writing – original draft; writing – review and editing; data curation. **Norman E. Davey:** Investigation; formal analysis; writing – review and editing; resources; data curation. **F. Emil Thomasen:** Investigation; software; formal analysis; writing – review and editing. **Nicholas Morffy:** Resources; writing – review and editing. **Andreas Prestel:** Formal analysis; writing – review and editing. **Inna Brakti:** Investigation; writing – review and editing. **Charlotte O'Shea:** Resources; writing – review and editing. **Lucia C. Strader:** Resources; writing – review and editing. **Kresten Lindorff-Larsen:** Supervision; funding acquisition; resources; writing – review and editing; methodology; software. **Karen Skriver:** Conceptualization; project administration; writing – review and editing; writing – original draft; resources; funding acquisition; validation. **Birthe B. Kragelund:** Conceptualization; supervision; funding acquisition; writing – original draft; writing – review and editing; resources; project administration; investigation; validation; methodology.

ACKNOWLEDGMENTS

The authors thank Dr. Izabella Krystkowiak, Dr. Frederik F. Theisen, and Steffie Elkjær for valuable discussions and Signe Sjørup for technical assistance. Acknowledgments are made to the DESY/EMBL P12 beamline at PETRA III facilities in Hamburg and beamline scientist Cy Jeffries for excellent assistance. The work was supported by the Novo Nordisk Foundation (grant no.: NNF18OC0032996 to B.B.K., cOpenNMR and grant no.: NNF18OC0033926 to B.B.K. and K.S. and no. NNF22OC0079339 to K.S.), Independent Research Fond Denmark (grant no.: 9040-00164B to BBK), Lundbeck Foundation BRAINSTRUC initiative grant (grant no.: R155-2015-2666 to K.L.-L. and B.B.K.), Villum Fonden for NMR equipment, and Cancer Research UK Senior Cancer Research Fellowship (grant no.: C68484/A28159 to N.E.D.).

CONFLICT OF INTEREST STATEMENT

KL-L holds stock options and is a consultant for Peptone Ltd. All other authors declare no competing interests.

DATA AVAILABILITY STATEMENT

The data that supports the findings of this study are available in the supplementary material of this article.

ORCID

Kresten Lindorff-Larsen https://orcid.org/0000-0002-4750-6039

Birthe B. Kragelund https://orcid.org/0000-0002-7454-1761

REFERENCES

Abramson J, Adler J, Dunger J, Evans R, Green T, Pritzel A, et al. Accurate structure prediction of biomolecular interactions with AlphaFold 3. Nature. 2024;630:493–500.

Akdel M, Pires DEV, Pardo EP, Jänes J, Zalevsky AO, Mészáros B, et al. A structural biology community assessment of AlphaFold2 applications. Nat Struct Mol Biol. 2022;29:1056–67.

Anderson JA, Glaser J, Glotzer SC. HOOMD-blue: a Python package for high-performance molecular dynamics and hard particle Monte Carlo simulations. Comput Mater Sci. 2020;173:109363.

Berlow RB, Dyson HJ, Wright PE. Hypersensitive termination of the hypoxic response by a disordered protein switch. Nature. 2017;543:447–51.

Bernadó P, Mylonas E, Petoukhov MV, Blackledge M, Svergun DI. Structural characterization of flexible proteins using small-angle x-ray scattering. J Am Chem Soc. 2007;129:5656–64.

Bjarnason S, McIvor JAP, Prestel A, Demény KS, Bullerjahn JT, Kragelund BB, et al. DNA binding redistributes activation domain ensemble and accessibility in pioneer factor Sox2. Nat Commun. 2024;15:1445.

Bottaro S, Bengtsen T, Lindorff-Larsen K. Integrating molecular simulation and experimental data: a Bayesian/maximum entropy reweighting approach. Methods Mol Biol. 2020;2112:219–40.

Broyles BK, Gutierrez AT, Maris TP, Coil DA, Wagner TM, Wang X, et al. Activation of gene expression by detergent-like protein domains. iScience. 2021;24:103017.

Bugge K, Staby L, Kemplen KR, O'Shea C, Bendsen SK, Jensen MK, et al. Structure of radical-induced cell Death1 hub domain

reveals a common *αα*-scaffold for disorder in transcriptional networks. Structure. 2018;26:734–746.e7.
Christensen LF, Staby L, Bugge K, O'Shea C, Kragelund BB, Skriver K. Evolutionary conservation of the intrinsic disorder-based radical-induced cell death1 hub interactome. Sci Rep. 2019;9:18927.
Davey NE, Edwards RJ, Shields DC. The SLiMDisc server: short, linear motif discovery in proteins. Nucleic Acids Res. 2007;35: W455–9.
Davey NE, van Roey K, Weatheritt RJ, Toedt G, Uyar B, Altenberg B, et al. Attributes of short linear motifs. Mol Biosyst. 2012;8: 268–81.
Delaforge E, Due AD, Theisen FF, Morffy N, O'Shea C, Blackledge M, et al. Allovalent scavenging of activation domains in the transcription factor ANAC013 gears transcriptional regulation. Nucleic Acids Res. 2025;53:gkaf065.
Delaglio F, Grzesiek S, Vuister GW, Zhu G, Pfeifer J, Bax A. NMRPipe: a multidimensional spectral processing system based on UNIX pipes. J Biomol NMR. 1995;6:277–93.
DelRosso N, Suzuki PH, Griffith D, Lotthammer JM, Novak B, Kocalar S, et al. High-throughput affinity measurements of direct interactions between activation domains and co-activators. bioRxiv [Internet]:2024.08.19.608698. 2024 https://doi.org/10.1101/2024.08.19.608698
Dreier JE, Prestel A, Martins JM, Brøndum SS, Nielsen O, Garbers AE, et al. A context-dependent and disordered ubiquitin-binding motif. Cell Mol Life Sci. 2022;79:484.
Erdős G, Pajkos M, Dosztányi Z. IUPred3: prediction of protein disorder enhanced with unambiguous experimental annotation and visualization of evolutionary conservation. Nucleic Acids Res. 2021;49:W297–303.
Erijman A, Kozlowski L, Sohrabi-Jahromi S, Fishburn J, Warfield L, Schreiber J, et al. A high-throughput screen for transcription activation domains reveals their sequence features and permits prediction by deep learning. Mol Cell. 2020;78:890–902.e6.
Flores E, Camacho AR, Cuevas-Zepeda E, McCoy MB, Yu F, Staller MV, et al. Correlating Disordered Activation Domain Ensembles with Gene Expression Levels.. Biophys Rep (NY). 2025; 5:100195.
Friis Theisen F, Salladini E, Davidsen R, Jo Rasmussen C, Staby L, Kragelund BB, et al. Aα-hub coregulator structure and flexibility determine transcription factor binding and selection in regulatory interactomes. J Biol Chem. 2022;298:101963.
Gianni S, Dogan J, Jemth P. Coupled binding and folding of intrinsically disordered proteins: what can we learn from kinetics? Curr Opin Struct Biol. 2016;36:18–24.
Gonçalves B, Hasson A, Belcram K, Cortizo M, Morin H, Nikovics K, et al. A conserved role for CUP-SHAPED COTYLEDON genes during ovule development. Plant J. 2015;83:732–42.
González-Foutel NS, Glavina J, Borcherds WM, Safranchik M, Barrera-Vilarmau S, Sagar A, et al. Conformational buffering underlies functional selection in intrinsically disordered protein regions. Nat Struct Mol Biol. 2022;29:781–90.
Grudinin S, Garkavenko M, Kazennov A. Pepsi-SAXS: an adaptive method for rapid and accurate computation of small-angle x-ray scattering profiles. Acta Crystallogr D Struct Biol. 2017;73: 449–64.
Hansen S. Bayesian estimation of hyperparameters for indirect Fourier transformation in small-angle scattering. J Appl Cryst. 2000; 33:1415–21.
Holehouse AS, Kragelund BB. The molecular basis for cellular function of intrinsically disordered protein regions. Nat Rev Mol Cell Biol. 2023;25:187–211.
Hummel NFC, Zhou A, Li B, Markel K, Ornelas IJ, Shih PM. The trans-regulatory landscape of gene networks in plants. Cell Syst. 2023;14:501–511.e4.
Ibrahim AY, Khaodeuanepheng NP, Amarasekara DL, Correia JJ, Lewis KA, Fitzkee NC, et al. Intrinsically disordered regions that drive phase separation form a robustly distinct protein class. J Biol Chem. 2023;299:102801.
Jehl P, Manguy J, Shields DC, Higgins DG, Davey NE. ProViz-a web-based visualization tool to investigate the functional and evolutionary features of protein sequences. Nucleic Acids Res. 2016; 44:W11–5.
Jensen MK, Kjaersgaard T, Nielsen MM, Galberg P, Petersen K, O'Shea C, et al. The *Arabidopsis thaliana* NAC transcription factor family: structure-function relationships and determinants of ANAC019 stress signalling. Biochem J. 2010;426:183–96.
Jin J, Tian F, Yang D-C, Meng Y-Q, Kong L, Luo J, et al. PlantTFDB 4.0: toward a central hub for transcription factors and regulatory interactions in plants. Nucleic Acids Res. 2017;45:D1040–5.
Jumper J, Evans R, Pritzel A, Green T, Figurnov M, Ronneberger O, et al. Highly accurate protein structure prediction with AlphaFold. Nature. 2021;596(7873):583–9.
Karlsson E, Schnatwinkel J, Paissoni C, Andersson E, Herrmann C, Camilloni C, et al. Disordered regions flanking the binding Interface modulate affinity between CBP and NCOA. J Mol Biol. 2022;434:167643.
Kim S-T, Lim D-S, Canman CE, Kastan MB. Substrate specificities and identification of putative substrates of ATM kinase family members. J Biol Chem. 1999;274:37538–43.
Kornberg RD. Mediator and the mechanism of transcriptional activation. Trends Biochem Sci. 2005;30:235–9.
Kotha SR, Staller MV. Clusters of acidic and hydrophobic residues can predict acidic transcriptional activation domains from protein sequence. Genetics. 2023;225:iyad131.
Krystkowiak I, Manguy J, Davey NE. PSSMSearch: a server for modeling, visualization, proteome-wide discovery and annotation of protein motif specificity determinants. Nucleic Acids Res. 2018;46:235–41.
Larsen AH, Pedersen MC. Experimental noise in small-angle scattering can be assessed using the Bayesian indirect Fourier transformation. J Appl Cryst. 2021;54:1281–9.
Liu J, Perumal NB, Oldfield CJ, Su EW, Uversky VN, Dunker AK. Intrinsic disorder in transcription factors. Biochemistry. 2006;45: 6873–88.
Lochhead MR, Brown AD, Kirlin AC, Chitayat S, Munro K, Findlay JE, et al. Structural insights into TAZ2 domain-mediated CBP/p300 recruitment by transactivation domain 1 of the lymphopoietic transcription factor E2A. J Biol Chem. 2020;295:4303–15.
Mahmood K, Zeisler-Diehl VV, Schreiber L, Bi Y-M, Rothstein SJ, Ranathunge K. Overexpression of ANAC046 promotes suberin biosynthesis in roots of *Arabidopsis thaliana*. Int J Mol Sci. 2019; 20:6117.
McGibbon RT, Beauchamp KA, Harrigan MP, Klein C, Swails JM, Hernández CX, et al. MDTraj: a modern open library for the analysis of molecular dynamics trajectories. Biophys J. 2015;109: 1528–32.
Millard PS, Bugge K, Marabini R, Boomsma W, Burow M, Kragelund BB. IDDomainSpotter: compositional bias reveals domains in long disordered protein regions—insights from transcription factors. Protein Sci. 2020;29:169–83. https://doi.org/10.1002/pro.3754
Mindel V, Brodsky S, Yung H, Manadre W, Barkai N. Revisiting the model for coactivator recruitment: Med15 can select its target sites independent of promoter-bound transcription factors. Nucleic Acids Res. 2024;52:12093–111. https://doi.org/10.1093/nar/gkae718
Morffy N, van den Broeck L, Miller C, Emenecker RJ, Bryant JA, Lee TM, et al. Identification of plant transcriptional activation domains. Nature. 2024;632:166–73.
Mulder FAA, Schipper D, Bott R, Boelens R. Altered flexibility in the substrate-binding site of related native and engineered high-alkaline *Bacillus subtilisins*. J Mol Biol. 1999;292:111–23.
Newcombe EA, Delaforge E, Hartmann-Petersen R, Skriver K, Kragelund BB. How phosphorylation impacts intrinsically

disordered proteins and their function. Essays Biochem. 2022; 66:901–13.

Newcombe EA, Due AD, Sottini A, Elkjær S, Theisen FF, Fernandes CB, et al. Stereochemistry in the disorder–order continuum of protein interactions. Nature. 2024;636:762–8.

Newcombe EA, Fernandes CB, Lundsgaard JE, Brakti I, Lindorff-Larsen K, Langkilde AE, et al. Insight into calcium-binding motifs of intrinsically disordered proteins. Biomolecules. 2021;11:1173.

Oda-Yamamizo C, Mitsuda N, Sakamoto S, Ogawa D, Ohme-Takagi M, Ohmiya A. The NAC transcription factor ANAC046 is a positive regulator of chlorophyll degradation and senescence in Arabidopsis leaves. Sci Rep. 2016;6:23609.

Olsen JG, Teilum K, Kragelund BB. Behaviour of intrinsically disordered proteins in protein–protein complexes with an emphasis on fuzziness. Cell Mol Life Sci. 2017;74:3175–83.

O'Shea C, Kryger M, Stender EGP, Kragelund BB, Willemoës M, Skriver K. Protein intrinsic disorder in *Arabidopsis* NAC transcription factors: transcriptional activation by ANAC013 and ANAC046 and their interactions with RCD1. Biochem J. 2015; 465:281–94.

O'Shea C, Staby L, Bendsen SK, Tidemand FG, Redsted A, Willemoës M, et al. Structures and short linear motif of disordered transcription factor regions provide clues to the interactome of the cellular hub protein radical-induced cell Death1. J Biol Chem. 2017;292:512–27.

Palopoli N, González Foutel NS, Gibson TJ, Chemes LB. Short linear motif core and flanking regions modulate retinoblastoma protein binding affinity and specificity. Protein Eng Des Sel. 2018;31: 69–77.

Pesce F, Lindorff-Larsen K. Refining conformational ensembles of flexible proteins against small-angle x-ray scattering data. Biophys J. 2021;120:5124–35.

Petoukhov MV, Franke D, Shkumatov AV, Tria G, Kikhney AG, Gajda M, et al. New developments in the ATSAS program package for small-angle scattering data analysis. J Appl Cryst. 2012; 45:342–50.

Prestel A, Wichmann N, Martins JM, Marabini R, Kassem N, Broendum SS, et al. The PCNA interaction motifs revisited: thinking outside the PIP-box. Cell Mol Life Sci. 2019;76: 4923–43.

Ptashne M, Gann A. Transcriptional activation by recruitment. Nature. 1997;386:569–77.

Ravarani CN, Erkina TY, de Baets G, Dudman DC, Erkine AM, Babu MM. High-throughput discovery of functional disordered regions: investigation of transactivation domains. Mol Syst Biol. 2018;14:e8190.

Rogers JM, Oleinikovas V, Shammas SL, Wong CT, de Sancho D, Baker CM, et al. Interplay between partner and ligand facilitates the folding and binding of an intrinsically disordered protein. Proc Natl Acad Sci USA. 2014;111:15420–5. https://doi.org/10.1073/pnas.1409122111

Rotkiewicz P, Skolnick J. Fast procedure for reconstruction of full-atom protein models from reduced representations. J Comput Chem. 2008;29:1460–5.

Sanborn AL, Yeh BT, Feigerle JT, Hao CV, Townshend RJ, Lieberman Aiden E, et al. Simple biochemical features underlie transcriptional activation domain diversity and dynamic, fuzzy binding to Mediator. Elife. 2021;10:e68068.

Shapiguzov A, Vainonen JP, Hunter K, Tossavainen H, Tiwari A, Järvi S, et al. *Arabidopsis* RCD1 coordinates chloroplast and mitochondrial functions through interaction with ANAC transcription factors. Elife. 2019;8:e43284.

Sievers F, Higgins DG. Clustal omega for making accurate alignments of many protein sequences. Protein Sci. 2018;27:135–45.

Sigler PB. Transcriptional activation. Acid blobs and negative noodles. Nature. 1988;333:210–2.

Singh KK, Graether SP. Expression and purification of an intrinsically disordered protein. Methods Mol Biol. 2020;2141:181–94.

Sjodt M, Clubb RT. Nitroxide labeling of proteins and the determination of paramagnetic relaxation derived distance restraints for NMR studies. Bio Protoc. 2017;7:e2207.

Skriver K, Theisen FF, Kragelund BB. Conformational entropy in molecular recognition of intrinsically disordered proteins. Curr Opin Struct Biol. 2023;83:102697.

Staby L, O'Shea C, Willemoës M, Theisen F, Kragelund BB, Skriver K. Eukaryotic transcription factors: paradigms of protein intrinsic disorder. Biochem J. 2017;474:2509–32.

Staller MV, Ramirez E, Kotha SR, Holehouse AS, Pappu RV, Cohen BA. Directed mutational scanning reveals a balance between acidic and hydrophobic residues in strong human activation domains. Cell Syst. 2022;13:334–345.e5.

Stender EG, O'Shea C, Skriver K. Subgroup-specific intrinsic disorder profiles of Arabidopsis NAC transcription factors: identification of functional hotspots. Plant Signal Behav. 2015;10: e1010967.

Taoka K, Yanagimoto Y, Daimon Y, Hibara K, Aida M, Tasaka M. The NAC domain mediates functional specificity of CUP-SHAPED COTYLEDON proteins. Plant J. 2004;40:462–73.

Teilum K, Kunze MBA, Erlendsson S, Kragelund BB. (S)Pinning down protein interactions by NMR. Protein Sci. 2017;26:436–51.

Tesei G, Lindorff-Larsen K. Improved predictions of phase behaviour of intrinsically disordered proteins by tuning the interaction range. Open Research Europe. 2023;2:94.

Tesei G, Martins JM, Kunze MBA, Wang Y, Crehuet R, Lindorff-Larsen K. DEER-PREdict: software for efficient calculation of spin-labeling EPR and NMR data from conformational ensembles. PLoS Comput Biol. 2021;17:e1008551.

Tesei G, Schulze TK, Crehuet R, Lindorff-Larsen K. Accurate model of liquid–liquid phase behavior of intrinsically disordered proteins from optimization of single-chain properties. Proc Natl Acad Sci USA. 2021;118(44):e2111696118. https://doi.org/10.1073/pnas.2111696118

Tesei G, Trolle AI, Jonsson N, Betz J, Knudsen FE, Pesce F, et al. Conformational ensembles of the human intrinsically disordered proteome. Nature. 2024;626:897–904.

Theisen FF, Prestel A, Elkjær S, Leurs YHA, Morffy N, Strader LC, et al. Molecular switching in transcription through splicing and proline-isomerization regulates stress responses in plants. Nat Commun. 2024;15:592.

Tuttle LM, Pacheco D, Warfield L, Wilburn DB, Hahn S, Klevit RE. Mediator subunit Med15 dictates the conserved "fuzzy" binding mechanism of yeast transcription activators Gal4 and Gcn4. Nat Commun. 2021;12:2220.

Udupa A, Kotha SR, Staller MV. Commonly asked questions about transcriptional activation domains. Curr Opin Struct Biol. 2024; 84:102732.

Virtanen P, Gommers R, Oliphant TE, Haberland M, Reddy T, Cournapeau D, et al. SciPy 1.0: fundamental algorithms for scientific computing in python. Nat Methods. 2020;17: 261–72.

von Bülow S, Tesei G, Lindorff-Larsen K. Prediction of phase separation propensities of disordered proteins from sequence. Natl Acad Sci USA. 2025; 122:e2417920122.

Vranken WF, Boucher W, Stevens TJ, Fogh RH, Pajon A, Llinas M, et al. The CCPN data model for NMR spectroscopy: development of a software pipeline. Proteins. 2005;59:687–96.

Wang ZX. An exact mathematical expression for describing competitive binding of two different ligands to a protein molecule. FEBS Lett. 1995;360:111–4.

Warfield L, Tuttle LM, Pacheco D, Klevit RE, Hahn S. A sequence-specific transcription activator motif and powerful synthetic variants that bind Mediator using a fuzzy protein interface. Proc Natl Acad Sci USA. 2014;111:E3506–13.

Wilson C, Lewis KA, Fitzkee NC, Hough LE, Whitten ST. ParSe 2.0: a web tool to identify drivers of protein phase separation at the proteome level. Protein Sci. 2023;32:e475.

Wirmer J, Peti W, Schwalbe H. Motional properties of unfolded ubiquitin: a model for a random coil protein. J Biomol NMR. 2006;35:175–86.

Wright PE, Dyson HJ. Intrinsically disordered proteins in cellular signalling and regulation. Nat Rev Mol Cell Biol. 2015;16:18–29.

SUPPORTING INFORMATION

Additional supporting information can be found online in the Supporting Information section at the end of this article.

How to cite this article: Due AD, Davey NE, Thomasen FE, Morffy N, Prestel A, Brakti I, et al. Hierarchy in regulator interactions with distant transcriptional activation domains empowers rheostatic regulation. Protein Science. 2025; 34(6):e70142. https://doi.org/10.1002/pro.70142